AIP | Journal of Applied Physics

Three-dimensional structure of (110) porous silicon with in-plane optical birefringence

Shinsuke Shichi, Minoru Fujii, Tomoki Nishida, Hidehiro Yasuda, Kenji Imakita et al.

Citation: J. Appl. Phys. **111**, 084303 (2012); doi: 10.1063/1.3703522
View online: http://dx.doi.org/10.1063/1.3703522
View Table of Contents: http://jap.aip.org/resource/1/JAPIAU/v111/i8
Published by the American Institute of Physics.

Three-dimensional structure of (110) porous silicon with in-plane optical birefringence

Shinsuke Shichi,[1] Minoru Fujii,[1,a)] Tomoki Nishida,[2] Hidehiro Yasuda,[2] Kenji Imakita,[1] and Shinji Hayashi[1]
[1]*Department of Electrical and Electronic Engineering, Graduate School of Engineering, Kobe University, Rokkodai, Nada, Kobe 657-8501, Japan*
[2]*Research Center for Ultra-HVEM, Osaka University, Mihogaoka 7-1, Ibaraki, Osaka 567-0047, Japan*

(Received 25 November 2011; accepted 9 March 2012; published online 16 April 2012)

Electrochemical etching of a (110) oriented Si wafer results in a porous silicon (PSi) layer which exhibits a strong in-plane optical birefringence. We study the refractive index ellipsoid of (110) PSi by angle-resolved optical transmittance measurements and reveal that it is a biaxial crystal. The angle-resolved transmission electron microscope observations demonstrate that pores grow along the directions in between the <100> crystal axes and the etching current flow and these directions depend on the etching current density. The etching current density dependence of the pore direction indicates that the shape of the index ellipsoid can be controlled by the etching condition. © *2012 American Institute of Physics*. [http://dx.doi.org/10.1063/1.3703522]

I. INTRODUCTION

Porous silicon (PSi) prepared from (110) Si wafers exhibits strong in-plane optical birefringence.[1–3] The refractive indices in the [001] ($n_{[001]}$) and $[1\bar{1}0]$ ($n_{[1\bar{1}0]}$) crystallographic directions can be controlled in a wide range by the etching current density.[4] Up to now, different kinds of polarizing elements such as waveplates,[5] polarizers,[6] and polarization dependent rugate filters and mirrors[7–9] operating in the visible to near infrared (NIR) ranges have been realized. Furthermore, wave plates for the ultraviolet range have been produced by birefringent porous silica made by the oxidation of birefringent PSi.[10]

The mechanism of the birefringence of (110) PSi is qualitatively explained by the alignment of Si nanowire skeletons constructing PSi along the <100> directions.[11–13] Kochergin *et al*. calculated the dielectric constant tensor of (110) PSi by assuming a model that the direction of pores coincides exactly with the equivalent <100> directions.[14,15] Bonder *et al*. calculated the polarization resolved refractive indices by a first-principle study of (110) PSi based on a super cell model. In the calculation, they assumed that elliptical columns of 1−4 atoms are removed from a Si crystal super cell of 16 atoms in the [100] and [010] directions.[16] Although these calculations assume the simplest structure for (110) PSi, it is not experimentally proved. In fact the three-dimensional structure of (110) PSi has not been experimentally analyzed. Furthermore, the index ellipsoid of (110) PSi is not determined; it is even not clear whether the index ellipsoid is uniaxial or biaxial. These information is indispensable to perform more realistic calculation and to improve the performance of (110) PSi polarizing elements.

In this work, we determine the shape of index ellipsoids of (110) PSi by angle-resolved optical transmittance measurements. We demonstrate that the ellipsoid is biaxial and the ellipticity depends on the etching current density. Following the optical measurements, we perform angle-resolved transmission electron microscopy (TEM) studies of the cross-sections of (110) PSi and study the direction of the pore growth. We discuss the mechanism of the in-plane optical birefringence based on the optical and TEM data.

II. EXPERIMENTAL PROCEDURES

(110) PSi was prepared by electrochemical etching of (110) oriented p^+ Si wafers (1−5 mΩ cm) in a solution of 1:1 by volume mixture of HF (46 wt. % in water) and ethanol. The etching current densities were 20, 50, and 80 mA/cm^2. At the end of the etching process, a high current pulse (300 mA/cm^2, 1.6 s) was applied to detach the PSi layer from the substrate.

Figure 1(a) shows a cleavage of a (110) Si wafer and the crystal axes. The long and short diagonals of the rhombus correspond to the directions of [001] and $[1\bar{1}0]$ crystal axes, respectively. Figure 1(b) shows a structural model of (110) PSi. Pores are schematically shown. The etching current flows to the [110] direction. For angle-resolved cross-sectional TEM observations, we prepare two specimens for each PSi sample, one with a (001) surface and the other with a $(1\bar{1}0)$ surface, by using a standard procedure including mechanical polishing and ion milling.

III. RESULTS AND DISCUSSION

A. Angle-resolved transmittance measurements

The setup for the angle-resolved optical transmittance measurements is shown in Fig. 1(c). Linearly polarized light (I_0) whose polarization direction is perpendicular to the rotation axis is incident on the sample, and the transmitted light with the same polarization direction is recorded in the wavelength range from 1000 to 2000 nm. This measurement is repeated by rotating the sample on the rotation axis. The rotation axis is either the [001] or $[1\bar{1}0]$ direction. The intensities of the transmitted light when the rotation axes are the

a)Author to whom correspondence should be addressed. Electronic mail: fujii@eedept.kobe-u.ac.jp.

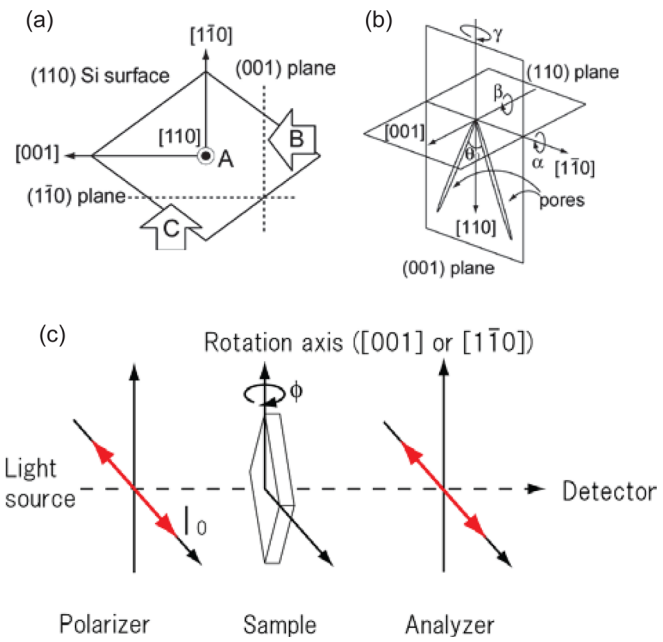

FIG. 1. (a), (b) Schematic illustrations of the structure of PSi. A, B, and C represent the direction of TEM observations. α, β, and γ represent rotation angles on [1$\bar{1}$0], [001] and [110] directions, respectively. (c) Experimental setup for the angle-resolved optical transmittance measurements. The polarization direction of incident light is perpendicular to the rotation axis. The rotation axis is either [001] and [1$\bar{1}$0] direction.

[1$\bar{1}$0] and [001] directions are denoted as $I(\phi_{[1\bar{1}0]})$ and $I(\phi_{[001]})$, respectively. Since the thickness of the samples (10 μm) is much larger than the wavelength of light, interference fringes appear in the spectra. From the interference fringes for the $I(\phi_{[1\bar{1}0]})$ and $I(\phi_{[001]})$ spectra, angle-dependence of the refractive indices, $n(\phi_{[1\bar{1}0]})$ and $n(\phi_{[001]})$, respectively, are obtained by the formula,

$$n(\phi) = \sqrt{\left[\frac{1}{2d}\left(\frac{1}{\lambda_r} - \frac{1}{\lambda_{r+1}}\right)^{-1}\right]^2 + \sin^2\phi}, \qquad (1)$$

where d is the thickness of the PSi film, λ_r is the wavelength of the rth fringe, and ϕ is the rotation angle.

Figure 2 shows refractive indices around 1300 nm as a function of the rotation angle ϕ. The data when the rotation axes are the [001] and [1$\bar{1}$0] directions are shown for the samples prepared with different etching current densities. The refractive indices are larger when the current density is smaller due to the smaller porosity. All the samples show birefringence ($n(\phi_{[001]}) > n(\phi_{[1\bar{1}0]})$).

If the index ellipsoid is uniaxial, either $n(\phi_{[1\bar{1}0]})$ or $n(\phi_{[001]})$ is independent of ϕ.[17] However, in Fig. 2, both $n(\phi_{[1\bar{1}0]})$ and $n(\phi_{[001]})$ increase with increasing the rotation angle. This indicates that the (110) PSi is a biaxial crystal. Refractive indices of the biaxial index ellipsoid can be expressed as

$$n(\phi'_{[001],([1\bar{1}0])}) = \sqrt{n^2_{[1\bar{1}0],([001])}\cos^2\phi' + n^2_{[110]}\sin^2\phi'}, \qquad (2)$$

where ϕ' is the refraction angle determined by the Snell's law.[17] The curves in Fig. 2 are the results of the fitting. We

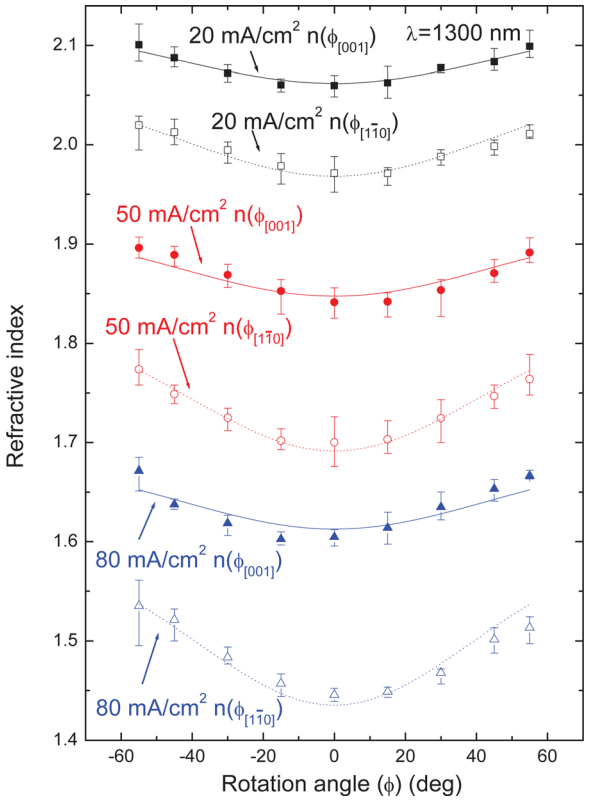

FIG. 2. Refractive indices as a function of rotation angle (ϕ) around 1300 nm. Filled and open symbols represent the refractive indices when the rotation axis is [001] and [1$\bar{1}$0] directions, respectively. Lines are the results of fitting. The etching current densities are 20, 50, and 80 mA/cm^2.

can see that experimental data can be well fitted by the equation. From the fitting, $n_{[001]}$, $n_{[1\bar{1}0]}$, and $n_{[110]}$ are obtained. Figure 3(a) shows $n_{[110]}$, $n_{[1\bar{1}0]}$, and $n_{[001]}$ as a function of the etching current density. $n_{[110]}$, $n_{[1\bar{1}0]}$, and $n_{[001]}$ have different

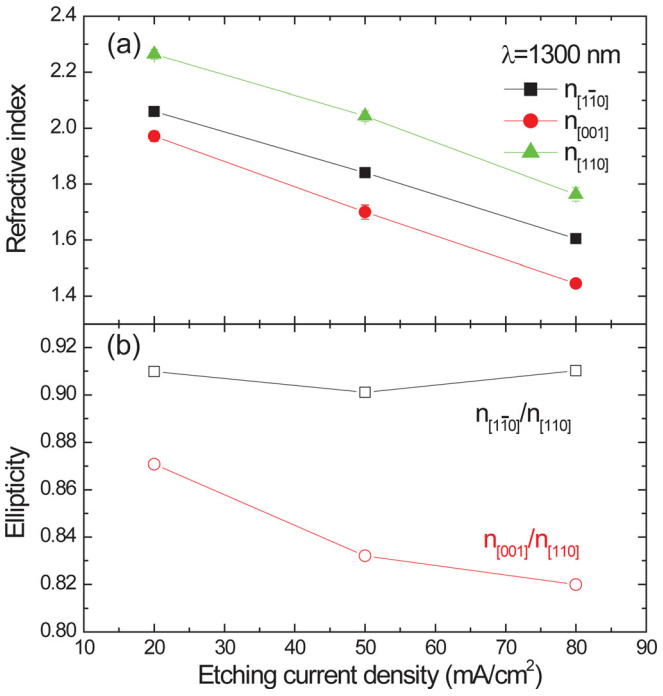

FIG. 3. Etching current density dependence of (a) refractive indices of [110], [1$\bar{1}$0] and [001] directions and (b) the ellipticities.

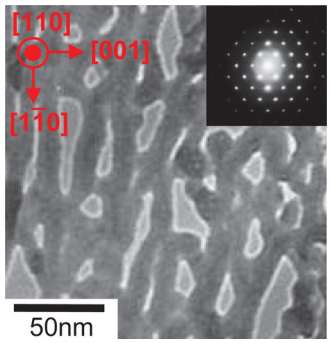

FIG. 4. Plan-view TEM image of (110) PSi with the etching current density of 80 mA/cm^2. The observation direction is "A" in Fig. 1(b). Inset is the electron diffraction pattern.

values for all the samples. This confirms that the (110) PSi is a biaxial crystal. The ellipticities represented by $n_{[1\bar{1}0]}/n_{[110]}$ and $n_{[001]}/n_{[110]}$ are shown in Fig. 3(b). $n_{[1\bar{1}0]}/n_{[110]}$ is almost constant, while $n_{[001]}/n_{[110]}$ decreases with increasing the etching current density. Therefore, the shape of the index ellipsoid depends on the etching current density. This suggests that we can design optical elements with different angular characteristics by properly choosing the etching current density range.

B. Angle-resolved TEM observations

Figure 4 shows a plan-view TEM image and a selected area electron diffraction (SAED) pattern of (110) PSi with the etching current density of 80 mA/cm^2. The observation direction corresponds to "A" in Fig. 1(a). The crystal axes

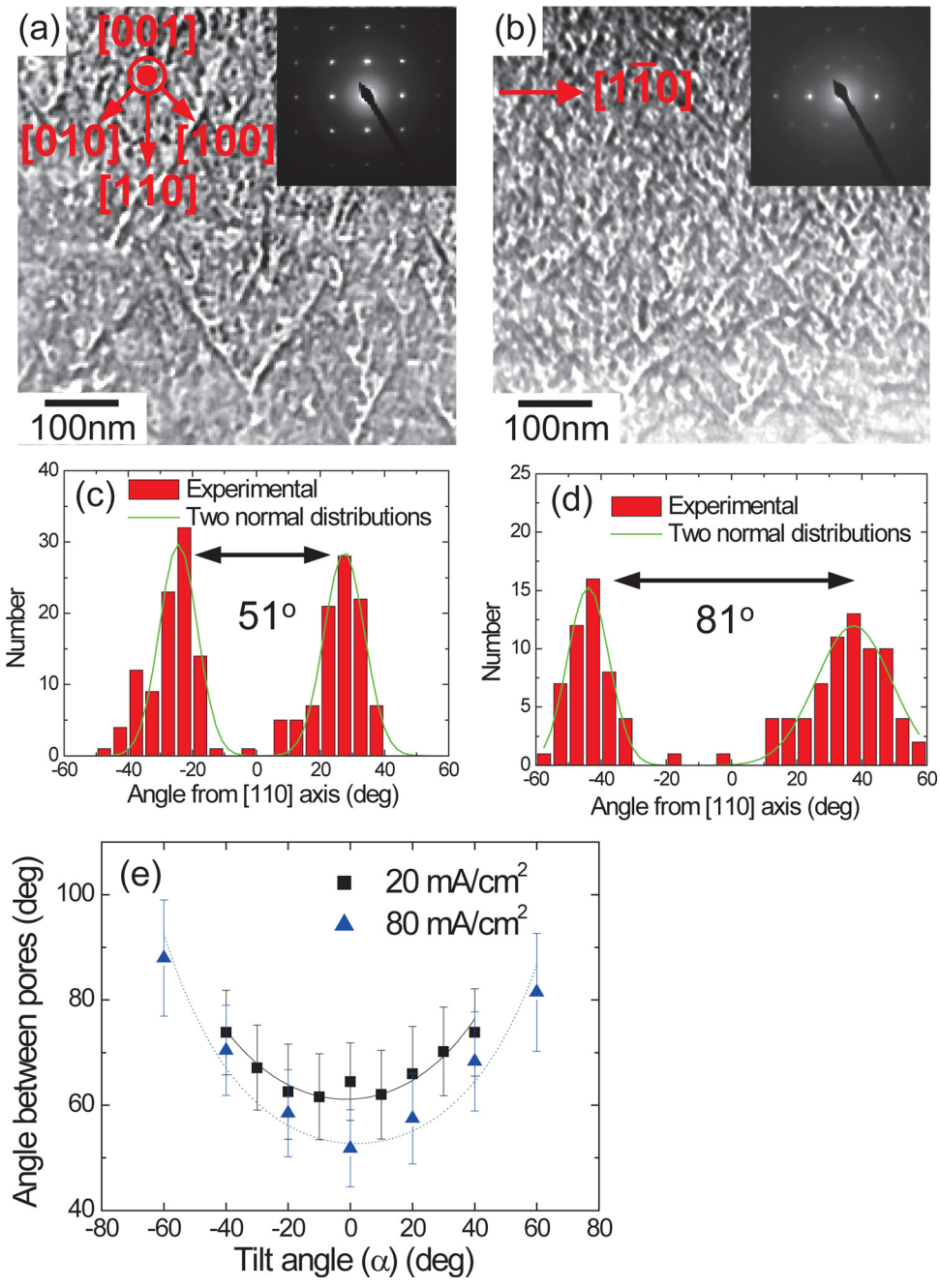

FIG. 5. (a) Cross-sectional TEM image with the [001] zone axis. The observation direction is "B" in Fig. 1(a). The sample is prepared with the etching current density of 80 mA/cm^2. (b) TEM image when the sample is tilted to the off-angle of 60° from the [001] zone axis on the [1$\bar{1}$0] axis as indicated by α in Fig. 1(b). Insets are the electron diffraction patterns. (c) and (d) Histograms of the inclination angles of pores to the [110] direction obtained from (a) and (b), respectively. (e) Tilt angle dependence of the angle between pores. The etching current densities are 20 and 80 mA/cm^2. The error bars are standard deviations of the distributions in (c) and (d).

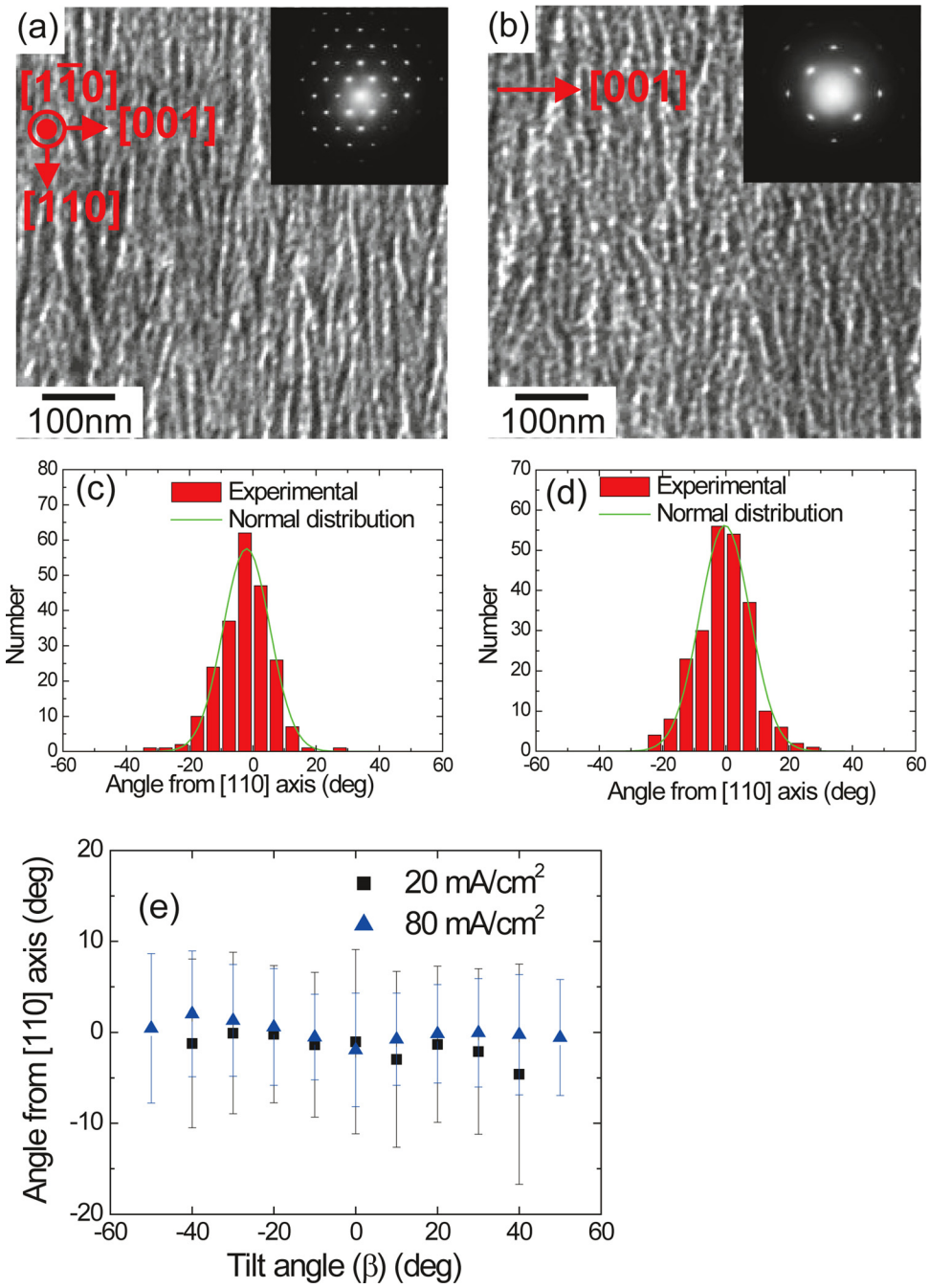

FIG. 6. (a) Cross-sectional TEM image with the [1$\bar{1}$0] zone axis. The observation direction is "C" in Fig. 1(a). The sample is prepared with the etching current density of 80 mA/cm^2. (b) TEM image when the sample is tilted to the off-angle of 50° from the [1$\bar{1}$0] zone axis on the [001] axis as indicated by β in Fig. 1(b). Insets are the electron diffraction patterns. (c) and (d) Histograms of the inclination angles of pores to the [110] direction obtained from (a) and (b), respectively. (e) Tilt angle dependence of the peak angles in the histograms. The etching current densities are 20 and 80 mA/cm^2. The error bars are standard deviations of the distributions in (c) and (d).

determined from the SAED are shown in the inset. The dark contrasts correspond to Si nanowire skeletons, while the bright regions to pores. The size (diameter) of the Si nanowires is several tens of nanometers. The pores and the Si nanowire skeletons align preferentially to the [1$\bar{1}$0] direction. This anisotropy of the structure is the origin of the in-plane birefringence. The SAED pattern indicates that the diamond structure of Si crystal is well-preserved and the (110) PSi is a single crystal.[18]

Figure 5(a) shows a cross-sectional TEM image with the [001] zone axis as indicated by the SAED in the inset. The observation direction is shown by arrow "B" in Fig. 1(a). The etching current flows from the top to the bottom. Bright contrasts corresponding to pores align along nearly the [100] and [010] directions. In order to qualitatively analyze the direction of the pore growth, we measure the inclination angles of pores to the [110] direction. The histogram of the angles is shown in Fig. 5(c). By fitting the histogram by two normal distribution functions, the average of the angles between pores aligned along two directions is obtained to be 51°.

In Fig. 5(b), the same sample is tilted to the off-angle of 60° from the [001] zone axis on the [1$\bar{1}$0] axis as indicated by α in Fig. 1(b). The bright contrasts shrink in length and only [2$\bar{2}$0] systematic reflections are conserved in the SAED. Figure 5(d) shows the histogram obtained from Fig. 5(b). The average angle between pores aligned along two directions increases to be approximately 81°. The same procedure is repeated at 20° intervals within the off-angles of ±60° from the [001] zone axis. The results are plotted in Fig. 5(e). The symbols represent the averages of the angles between

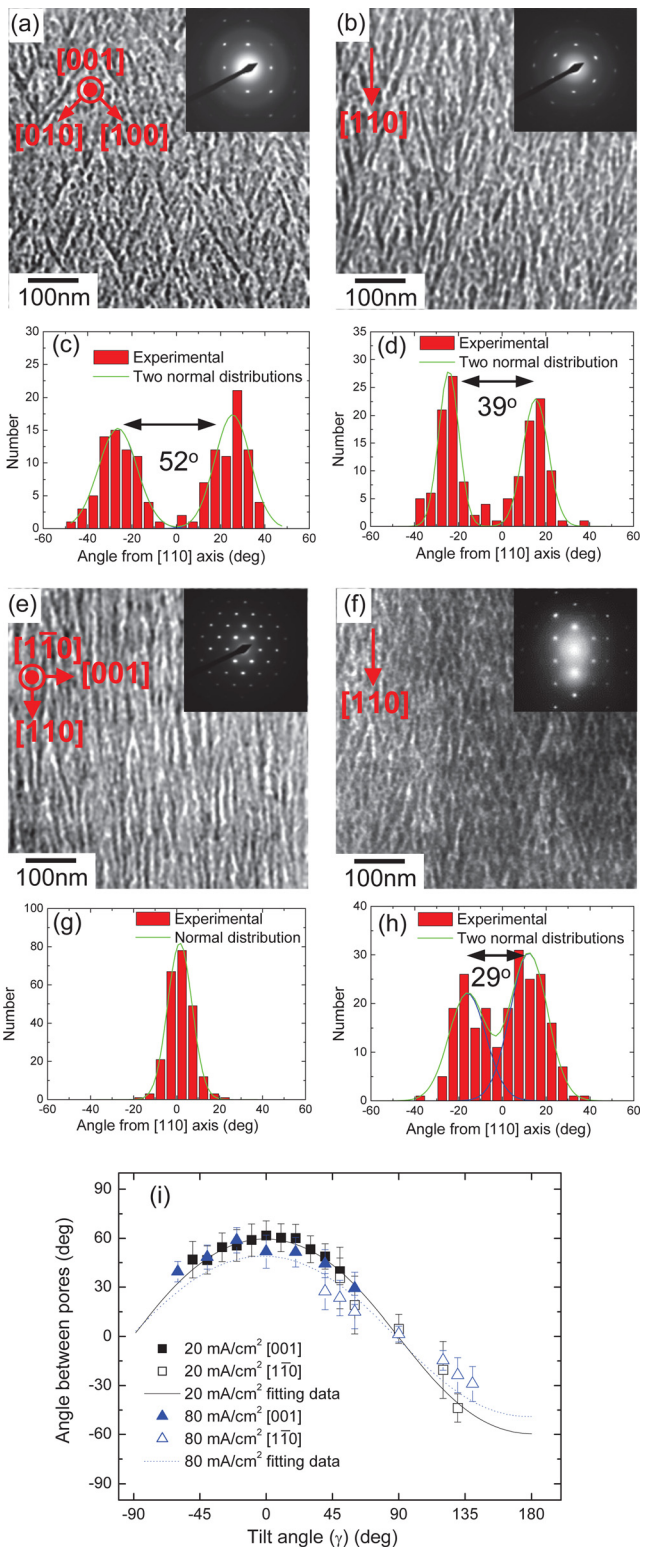

FIG. 7. (a) Cross-sectional TEM image with the [001] zone axis. The sample is prepared with the etching current density of 80 mA/cm^2. (b) TEM image when the sample is tilted to the off-angle of 60° from the [001] zone axis on the [110] axis as indicated by γ in Fig. 1(b). (c) and (d) Histograms of the inclination angles of pores to the [110] direction obtained from (a) and (b), respectively. (e) Cross-sectional TEM image with the [1$\bar{1}$0] zone axis. (f) TEM image when the sample is tilted to the off-angle of 50° from the [1$\bar{1}$0] zone axis on the [110] axis as indicated by γ in Fig. 1(b). (g) and (h) Histograms of the inclination angles of pores to the [110] direction obtained from (e) and (f), respectively. (i) Tilt angle dependence of the angle between pores. The tile angle γ represents the angle measured from the [001] axis. The etching current densities are 20 and 80 mA/cm^2.

the pores and the error bars are standard deviations of the distributions in the histograms. In Fig. 5(e), the data obtained for the samples prepared with the etching current densities of 20 and 80 mA/cm^2 are shown. Figure 5(e) demonstrates that the angle between pores is different between the two samples prepared with different etching current densities.

The tilt angle α dependence of the angle between pores is expressed from a simple geometrical consideration by

$$\theta = 2\arctan\left(\frac{\tan\frac{\theta_0}{2}}{\cos(\alpha-\alpha_0)}\right), \tag{3}$$

where θ is the angle between pores, α is the tilt angle, θ_0 is the minimum of θ, α_0 is the tilt angle when $\theta=\theta_0$. The definition of these angles is shown in Fig. 1(b). In Fig. 5(e), the data are well-fitted by this simple equation. When the etching current density is 20 mA/cm^2, θ_0 and α_0 obtained by the fitting are 61° and −2°, respectively, while when it is 80 mA/cm^2, they are 53° and 1.7°, respectively. The small α_0 implies that pores are in the (001) plane as schematically shown in Fig. 1(b) within the accuracy of the present work. Furthermore, different values of θ_0 confirm that the direction of pores depends on the etching current density.

Figure 6(a) shows a cross-sectional TEM image with the [1$\bar{1}$0] zone axis as indicated by the SAED in the inset. The observation direction is shown by arrow "C" in Fig. 1(a). Bright contrasts corresponding to pores grow along the direction almost parallel to the current flow. Figure 6(c) shows the histogram of the inclination angles of pores to the [110] direction obtained from Fig. 6(a). A single peak appears in the histogram and the peak angle obtained by the normal distribution function fitting is −2°. The TEM image and the histogram obtained when the sample is tilted to the off-angle of 50° from the [1$\bar{1}$0] zone axis on the [001] axis [β in Fig. 1(b)] are shown in Figs. 6(b) and 6(d), respectively. Similar to Fig. 6(a), pores grow almost parallel to the [110] direction. The same procedure is repeated at 10° intervals within the off-angles of ±50° from the [1$\bar{1}$0] zone axis. The peak angles of the histograms are plotted as a function of the tilt angle β in Fig. 6(e) for the samples prepared with the etching current densities of 20 and 80 mA/cm^2. Regardless of the etching current density and the tilt angle, the inclination angles of pores to the [110] direction are almost 0°. This also confirms that the pores exist in the (001) plane irrespective of the etching current density.

In order to determine the direction of pore growth more precisely, we repeat similar procedure by tilting the samples on the [110] axis. Figure 7(a) shows a cross-sectional TEM image with the [001] zone axis. In Fig. 7(b), the same sample is tilted to the off-angle of 60° from the [001] zone axis on the [110] axis [γ in Fig. 1(b)]. The corresponding histograms of pore directions are shown in Figs. 7(c) and 7(d), respectively. By fitting the histograms by two normal distribution functions, the angles between the peaks in the histograms are obtained to be 52° and 39°, respectively. Figure 7(e) shows a cross-sectional TEM image with the [1$\bar{1}$0] zone axis. The TEM image when the sample is tilted to the off-angle of 50°

from the $[1\bar{1}0]$ zone axis on the [110] axis is shown in Fig. 7(f). The corresponding histograms are shown in Figs. 7(g) and 7(h) and the angles between pores obtained by fitting the histograms are 0° and 29°, respectively.

The analyses are repeated within the off-angles of ±60° from the [001] zone axis and ±50° from the $[1\bar{1}0]$ zone axis on the [110] axis. The results are plotted in Fig. 7(i). Note that the tile angle γ represents the angle measured from the [001] axis. The square and triangle symbols correspond to the samples prepared with the etching current densities of 20 and 80 mA/cm^2, respectively. Closed squares and triangles represent the data obtained by tilting the samples from the [001] zone axis and open ones those obtained by tilting the samples from the $[1\bar{1}0]$ zone axis. In Fig. 7(i), we can see that the angle between pores is different between the samples prepared with different etching current densities. From the simple geometrical consideration, γ dependence of the angles between pores is expressed as

$$\theta = 2\arctan\left(\tan\frac{\theta_0}{2}\cos(\gamma-\gamma_0)\right). \quad (4)$$

The data in Fig. 7(i) can be well-fitted by the formula and from the fitting, θ_0 and γ_0 are obtained. When the etching current density is 20 mA/cm^2, $\theta_0 = 60°$ and $\gamma_0 = -2°$, and when it is 80 mA/cm^2, $\theta_0 = 50°$ and $\gamma_0 = -0.5°$. From these analyses, it is now clear that the direction of pore growth does not coincide with the <100> directions and the degree of the deviation from the <100> directions depends on the etching current density.

It is well-known that in alkaline etching of Si crystal, the ratio of the etching rates for the (100), (110), and (111) planes are 100:16:1.[19] As a result, the alkaline etching of (110) Si proceeds preferentially to <100> directions. In metal-assisted chemical etching of (110) Si wafer without current flow, Si is preferentially etched to the [100] and [010] directions.[20,21] This results in the growth of pores to the [100] and [010] directions and the angles between pores become 90°. The deviation of the angles θ_0 from 90° observed in this work indicates that in the electrochemical etching process, the direction of pore growth is determined by crystallographic directions and the direction of current flow.

When pores grow along the [100] and [010] directions and the angles between pores are 90°, the index ellipsoid becomes uniaxial. On the other hand, when the directions deviates from the [100] and [010] directions, it becomes biaxial. Therefore, the TEM results that θ_0 is 60° and 50° are consistent with the optical data in Fig. 3, which suggest biaxial index ellipsoid. Furthermore, the result that the shape of the ellipsoid depends on the etching current density can also be explained by the etching current dependence of the pore directions.

IV. CONCLUSIONS

We study the three-dimensional structures and the index ellipsoids of (110) PSi by angle-resolved TEM observations and optical transmittance measurements. It is found that the direction of pore growth does not coincide with the <100> directions and it approaches to the direction of current flow when the etching current density increases. This result is different from the model structure of (110) PSi used for theoretical calculations. The present results indicate that the structure of (110) PSi is more complex than expected and to perform more realistic calculation, the information obtained in this work should be included. We also show by angle-resolved optical transmittance measurements that the index ellipsoids are biaxial and the shape of the ellipsoids depends on the etching current density. This result is consistent with the pore structures obtained from TEM observations. The present work suggests that the shape of index ellipsoid of (110) PSi can be controlled by the etching current density, and thus optical elements with different angular characteristics can be produced by properly choosing the etching current density range.

ACKNOWLEDGMENTS

This work is supported by "Nanotechnology Network Project of the Ministry of Education, Culture, Sports, Science and Technology (MEXT), Japan" at the Research Center for Ultrahigh Voltage Electron Microscopy, Osaka University (Handai multi-functional Nano-Foundry).

[1]N. Künzner, D. Kovalev, J. Diener, E. Gross, V. Y. Timoshenko, G. Polisski, F. Koch, and M. Fujii, Opt. Lett. **26**, 1265 (2001).
[2]O. G. Sarbey, E. K. Frolova, R. D. Fedorovich, and D. B. Dan'ko, Phys. Solid State **42**, 1240 (2000).
[3]L. A. Golovan, P. K. Kashkarov, and V. Y. Timoshenko, Crystallogr. Rep. **52**, 672 (2007).
[4]N. Künzner, J. Diener, E. Gross, D. Kovalev, V. Y. Timoshenko, and M. Fujii, Phys. Rev. B **71**, 195304 (2005).
[5]D. Kovalev, G. Polisski, J. Diener, H. Heckler, N. Künzner, V. Y. Timoshenko, and F. Koch, Appl. Phys. Lett. **78**, 916 (2001).
[6]J. Diener, N. Künzner, E. Gross, D. Kovalev, and M. Fujii, Opt. Lett. **29**, 195 (2004).
[7]N. Ishikura, M. Fujii, K. Nishida, S. Hayashi, and J. Diener, Opt. Express **16**, 15531 (2008).
[8]J. Diener, N. Künzner, D. Kovalev, E. Gross, V. Y. Timoshenko, G. Polisski, and F. Koch, Appl. Phys. Lett. **78**, 3887 (2001).
[9]J. Diener, N. Künzner, D. Kovalev, E. Gross, F. Koch, and M. Fujii, J. Appl. Phys. **91**, 6704 (2002).
[10]S. Shichi, M. Fujii, and S. Hayashi, Opt. Lett. **36**, 3951 (2011).
[11]S. F. Chuang, S. D. Collins, and R. L. Smith, Appl. Phys. Lett. **55**, 675 (1989).
[12]V. Lehmann and S. Ronnebeck, J. Electrochem. Soc. **146**, 2968 (1999).
[13]R. L. Smith and S. D. Collins, J. Appl. Phys. **71**, R1 (1992).
[14]V. Kochergin, M. Christophersen, and H. Foll, Appl. Phys. B **79**, 731 (2004).
[15]V. Kochergin, M. Christophersen, and H. Foll, Appl. Phys. B **80**, 81 (2005).
[16]Y. Bonder and C. M. Wang, J. Appl. Phys. **100**, (2006).
[17]J. M. Liu, *Photonic Devices* (Cambridge University Press, 2005).
[18]A. G. Cullis, L. T. Canham, and P. D. J. Calcott, J. Appl. Phys. **82**, 909 (1997).
[19]S. M. Sze, *Semiconductor Devices: Physics and Technology* (Wiley, 1985).
[20]Z. P. Huang, T. Shimizu, S. Senz, Z. Zhang, X. X. Zhang, W. Lee, N. Geyer, and U. Gösele, Nano Lett. **9**, 2519 (2009).
[21]Z. P. Huang, N. Geyer, P. Werner, J. de Boor, and U. Gösele, Adv. Mater. **23**, 285 (2011).